

Highlights

An Explainable-AI Approach for Diagnosis of COVID-19 using MALDI-ToF Mass Spectrometry

Venkata Devesh Reddy Seethi,Zane LaCasse,Prajakta Chivte,Joshua Bland,Shrihari S. Kadkol,Elizabeth R. Gaillard,Pratool Bharti,Hamed Alhoori

- Trained an AI model with human oral gargle sample data analyzed by MALDI MS method.
- Achieved a high accuracy in COVID-19 diagnosis.
- Incorporated X-AI techniques to explain the reasoning behind the outcomes from AI models from different perspectives.

An Explainable-AI Approach for Diagnosis of COVID-19 using MALDI-ToF Mass Spectrometry

Venkata Devesh Reddy Seethi^a, Zane LaCasse^a, Prajкта Chivte^a, Joshua Bland^b, Shrihari S. Kadkol^b, Elizabeth R. Gaillard^a, Pratoool Bharti^c and Hamed Alhoori^a

^aNorthern Illinois University, Dekalb, Illinois, 60115, USA

^bUniversity of Illinois Chicago, Chicago, Illinois, 60612, USA

^cIntel Corporation, Hillsboro, Oregon, 97124, USA

ARTICLE INFO

Keywords:

COVID-19 testing
Explainable-AI
Machine learning
RT-PCR test
Mass spectrometry
MALDI-ToF

ABSTRACT


The severe acute respiratory syndrome coronavirus type-2 (SARS-CoV-2) caused a global pandemic and imposed immense effects on the global economy. Accurate, cost-effective, and quick tests have proven substantial in identifying infected people and mitigating the spread. Recently, multiple alternative platforms for testing coronavirus disease 2019 (COVID-19) have been published that show high agreement with current gold standard real-time polymerase chain reaction (RT-PCR) results. These new methods do away with nasopharyngeal (NP) swabs, eliminate the need for complicated reagents, and reduce the burden on RT-PCR test reagent supply. In the present work, we have designed an artificial intelligence-based (AI) testing method to provide confidence in the results. Current AI applications to COVID-19 studies often lack a biological foundation in the decision-making process, and our AI approach is one of the earliest to leverage explainable-AI (X-AI) algorithms for COVID-19 diagnosis using mass spectrometry. Here, we have employed X-AI to explain the decision-making process on a local (per-sample) and global (all samples) basis underscored by biologically relevant features. We evaluated our technique with data extracted from human gargle samples and achieved a testing accuracy of 94.44%. Such techniques would strengthen the relationship between AI and clinical diagnostics by providing biomedical researchers and healthcare workers with trustworthy and, most importantly, explainable test results.

1. Introduction

The virulent, fast-spreading, and mutating nature of SARS-CoV-2 caused a worldwide pandemic with more than 662 million people infected, and 6.7 million lives were taken in the span of 3 years since emerging [1]. This pandemic has challenged the ability of healthcare systems to triage patients and overwhelmed capacities. Beyond healthcare, societal impacts have been apparent, and major sectors of the global economy have been affected [2]. Given the severity of the pandemic and the emergence of new variants of SARS-CoV-2 [3], curbing the infection caused by the virus has become a major concern for all nations. Several protocols have been implemented, such as vaccinations, mask mandates, and lockdowns, to reduce the spread of the virus. Frequent and rapid surveillance testing, nonetheless, remains the key critical factor in reducing the transmission of the virus [4]. As COVID-19 exhibits a broad range of clinical manifestations, from mild fever to life-threatening conditions, it is critical to implement testing protocols for its early diagnosis in order to curb viral transmission. Molecular detection of SARS-CoV-2 predominantly relies on the current gold standard Real-time Polymerase Chain Reaction (RT-PCR) technique for viral RNA identification. Despite ongoing COVID-19 testing advancements, there is still a significant trade-off between testing specificity and complexity.

Although RT-PCR protocols have achieved high specificities of 95.2% [5], completely relying on RT-PCR will make it a labor-intensive process with limited skilled personnel and exert a huge strain on laboratory reagents for the testing process [6]. Various other alternatives for detecting SARS-CoV-2 nucleic acids, such as isothermal amplification assays, amplicon-based metagenomic sequencing, hybridization using microarray and CRISPR-based technologies, are simultaneously being developed to meet the unprecedented demands for a rapid but reliable testing platform [5, 6, 7, 8]. Approximately 400 rapid diagnostic tests are commercially available, amongst which lateral flow devices are the most prominent ones and provide up to 70% sensitivity to detect antibodies [9].

Matrix-Assisted Laser Desorption/Ionization Time-of-Flight (MALDI-ToF) has become one of the leading proteomic tools due to its minimal sample preparation, tolerance for matrix contaminants, and rapid analysis providing multi-dimensional information [10, 11, 12]. Previous research reported a MALDI-ToF-based method for profiling proteins in gargle samples where both host and viral proteins are observed. This study included samples from people whose COVID-19 status was verified with RT-PCR testing. Utilizing straight-forward area under the curve (AUC) analysis of protein signals in the MALDI-ToF spectra, the method achieved overall above 90% specificity and sensitivity (recall) rates [13]. In this study, we used data from Chivte et al. [13] with newly collected samples. However, an in-depth look at the spectra shows that they are fairly complicated, with a multitude of signals detected from both host immune response proteins and viral proteins. The

 dseethi@niu.edu (V.D.R. Seethi); zlacasse1@niu.edu (Z. LaCasse); pchivte@niu.edu (P. Chivte); jbland3@uic.edu (J. Bland); skadkol@uic.edu (S.S. Kadkol); gaillard@niu.edu (E.R. Gaillard); pratoool.bharti@intel.com (P. Bharti); alhoori@niu.edu (H. Alhoori)

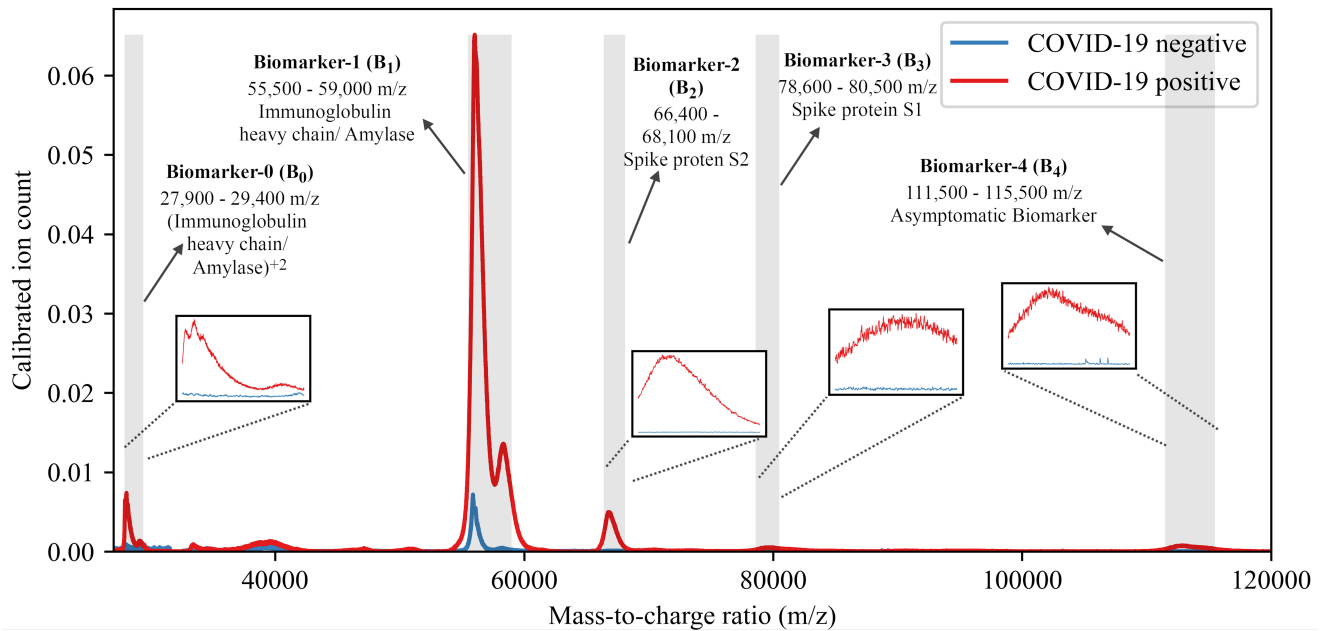


Figure 1: Comparison of COVID-19 negative and a COVID-19 positive gargle MALDI-ToF spectra after preprocessing with baseline correction and normalization. Regions of interest of different Biomarkers in the spectra are highlighted with a gray hue. Zoom-in panels for each range show differences between the disease statuses.

amounts of these proteins change over the course of an infection's lifecycle, further confounding the data in the spectra. Thus, we now report on an alternative analysis using X-AI algorithms.

We designed our AI-based approach to learn the relationships between the intensity of the proteins and the outcome of an RT-PCR test. When AI systems learn a complex pattern, their decision-making process is often opaque and uninterpretable, resulting in a black-box system. In clinical settings, black-box systems pose an impossible task for domain experts and health practitioners to understand the factors contributing to a test's outcome. Therefore, we tackle this problem using X-AI techniques that document the decision-making process in transferring a mass spectral dataset into a COVID-19 diagnosis. Even though the decision-making process of the AI system is complex, the explanations are easy to understand, which aids a clinician in interpreting the reasons for a diagnosis. This characteristic is analogous to a real-time diagnosis, where doctors explain to patients what markers lead to their final diagnosis. Therefore, having the model interpretable is critical as it makes the system transparent and instills trust in our AI system.

2. LITERATURE REVIEW

Machine learning algorithms have become an integral part of research in COVID-19 diagnostic protocols [14]. As mentioned in Section 1 a wide range of protocols have been studied that use different sample collection processes, feature engineering techniques, and machine learning algorithms. Previous mass spectrometry studies adopted feature engi-

neering techniques such as area under the curve (i.e., summation of all intensities) or peaks (i.e., local maximas). Among the studies that use NP swabs, Nachtigall et al. [15] collected 362 samples that were analyzed by MALDI-MS in the mass-to-charge range 3 – 15.5 kDa. Spectral peaks were extracted by filtering local maxima, followed by correlation-based and impurity-based feature selection methods to identify 88 important peaks that discriminate between COVID-19 positive and negative samples. They achieved 93.9% accuracy with the support vector machine (SVM) algorithms [16]. Rocca et al. [17] collected 311 samples and conducted several statistical tests [17] to select characteristic peaks, and their k-nearest neighbor classifier achieved an accuracy of approximately 90%. In other work, Tran et al. [18] collected 199 samples, extracted peaks, and optimized their AI solution using machine intelligence learning optimizer (MILO) [19]. MILO builds an end-to-end pipeline that automatically selects the best features and tunes hyperparameters for algorithms [19]. The results of MILO showed extreme gradient boosting (XgBoost) [20], and the deep neural network (DNN) [21] algorithms performed best with 98.3% accuracy. In a more recent study, Deulofeu et al. [22] collected two datasets with 148 and 66 samples using different sample processing techniques. The authors generated 5-50 principal components from the peaks dataset using principal component analysis [23] and reported the accuracies as 70.3% with XgBoost and 88.4% with SVM for their two datasets, respectively.

Alternative to NP swabs, Yan et al. [24] collected 298 serum samples. In feature processing, Yan et al. selected 50 peaks where 20, 20, 10 peaks were determined using

LASSO [25], partial least-squares-discriminant analysis [26], and recursive feature elimination with cross-validation [27], respectively. As a next step, they conducted empirical analysis, picked 25 relevant peaks from the 50 peaks, and found that logistic regression gave the best accuracy of 99%. Costa et al. [28] explored the efficacy of saliva samples in COVID-19 testing and collected 360 samples. Costa et al. further extracted and selected nine statistically significant peaks with the Wilcoxon rank sum test and Benjamini–Hochberg [29] correction. Lastly, their SVM algorithm exhibited the best performance with accuracy ranging from 64.3% – 88.9%.

More recently, researchers adopted AI approaches driven by X-AI [30] analysis in COVID-19 detection for different datasets such as blood samples [24, 31, 32, 33, 34], CT scans [35, 36, 37, 38], and X-Rays [39, 40, 41, 42, 43, 44, 45]. Rahman et al. [46] used multimodal data from X-Rays, CT scans, cough audio data, and facial recognition and attempted to create an ensemble pipeline with multiple point-of-care premise tools to detect COVID-19. Some studies also explored forecasting COVID-19 cases by learning the time-series relationship between the historical data, such as transmission, and recovery rates, to forecast case numbers or chances of getting infected with COVID-19 [47, 48, 49]. Smith et al. [50] identified mortality factors of patients in a hospital by training a model on tabular data with features such as age, gender, and lymphocyte count and presented the features that had a high contribution towards a patient's mortality using XAI techniques. Furthermore, explainable AI has been used in spectrometry datasets for biomarker discovery [51] and cell classification [52], and has also shown potential in learning age group-dependent features in COVID-19 [53]. Most of the previous X-AI studies are based on datasets that are tabular or 2D images. In general, tabular data is a set of rows and columns, while image data can be either a 2D X-ray scan or a CT scan. By looking at previous studies in X-AI, it is apparent that SHAP [54, 55] was the best-known method for tabular datasets and decision trees [56] for building transparent models with tree-based explanations [34]. On the other hand, for image datasets, GRAD-CAM [57] and SCORE-CAM [58] techniques were more popular. In this study, we demonstrate an X-AI framework leveraging mass spectrometry data generated from gargle samples. We also outline and show the application of several X-AI strategies that were proponents of making the AI-methods trustworthy in previous studies.

3. CONTRIBUTIONS

In our current work, we incorporate one of the newest sample collection processes known for cost-effectiveness and ease of implementation. We also present a thorough evaluation of our feature processing technique as well as from the previous mass spectrometry literature. Furthermore, we also demonstrate that the diagnosis becomes feasible and accurate with the integration of AI algorithms. We additionally interpret the AI algorithm to provide informed explanations of diagnosis, leverage a cost-effective and easy-to-use MALDI-ToF MS approach, and use a non-invasive speci-

men type (saliva). After assessing multiple AI approaches, we built our AI solution based on a tree-based ensemble algorithm (Random Forest [59]) using MALDI-ToF MS data. We showed that when the confidence in our Random Forest model predictions is high, it is highly accurate and can act as a gatekeeper to reduce the usage of PCR tests in cases where model confidence is high. Next, we calibrated the trained algorithm and interpreted the predictions using X-AI techniques such as SHAP, impurity-based feature importance, and permutation feature importance.

4. DATASET PREPARATION

4.1. Data Collection

Samples were collected from the students at Northern Illinois University in August and September 2020. Ethical approval was issued by the Institutional Review Board. All participants provided written consent before participating in the research study. Students who consented to participate in the research study were asked to provide a water gargle sample at the same time as the NP swab sample collection. After sample collection, we processed the samples as described below while NP swabs were subjected to RT-PCR testing conducted near the University. For each gargle sample, we used the outcome of the RT-PCR test with an NP swab as ground truth in our analyses. We analyzed 152 gargle samples, including 60 COVID-19 positives and 92 COVID-19 negatives.

In brief, participants gargled 10 mL of bottled spring water for 30 seconds and deposited the gargled sample in a 50 mL conical centrifuge tube. We then filtered the gargled sample and collected the specimen through a 0.45 μ m syringe filter, used acetone precipitation to concentrate proteins, centrifuged, and resuspended the pellet in a reconstitution buffer. After incubation, we spotted each sample on a target plate, air-dried, and transferred the plate to a Shimadzu AXIMA Performance [60] mass spectrometer, which was calibrated with a protein standard daily. Ions were detected in a positive-ion, linear detection mode over a range of 2,000 – 200,000 m/z. Finally, we corrected the baseline of all the generated spectra using the Shimadzu Launchpad software obtained from the manufacturer [60] and normalized the ion count intensities with the parent peak of the protein standard calibrant.

4.2. Potential Biomarker Selection

The presence or absence of intensities in the collected mass spectra can be correlated to the presence or abundance of proteins within each specimen. The spectra collected represent a multitude of proteins (in this case, after acetone precipitation) that are in the range of 2,000 – 200,000 m/z. In mass spectrometry, we measure large molecules that have a distribution over a range of m/z values instead of a single m/z value. While our goal was to distinguish between a positive and negative sample, we selected m/z ranges identified by researchers in [13] that were observed to change given the COVID-19 status by RT-PCR.

Biomarker	Mass Range (m/z)	Potential Identity
B_0	27,900 – 29,400	Human Protein-1
B_1	55,500 – 59,000	Human Protein-2
B_2	66,400 – 68,100	Viral Protein-1
B_3	78,600 – 80,500	Viral Protein-2
B_4	111,500 – 115,500	Human Protein-3

Table 1
Potential biomarker ranges and their descriptions.

An overlay of mass spectra highlighting these differences for a COVID-19 positive and negative sample is shown in Figure 1. Note that Figure 1 only shows a segment of the spectra where potential COVID-19 biomarkers are present. These biomarker peaks were selected to potentially include both human proteins (i.e., immunoglobulin heavy chain, amylase, asymptomatic biomarker) and SARS-CoV-2 viral proteins (Spike protein subunits S2 and S1). For the sake of simplicity, here, these ranges were named Human Protein-1 (HP1), Human Protein-2 (HP2), Human Protein-3 (HP3), and Viral Protein-1 (VP1), Viral Protein-2 (VP2), respectively. We provide a summary of the biomarkers and their mass ranges in Table 1.

4.3. Feature Engineering

The performance of supervised ML algorithms depends on the quality of the features used in training. In general, an AI model becomes more robust as the number of features increases and weakens due to overfitting after a certain number [61]. We thus conduct a holistic analysis of feature processing techniques such as raw spectral data, peaks in spectra, statistical features, the area under the curve (AUC), arithmetic permutations without repetition of AUC features, and statistical hand-crafted features. We implemented all feature engineering techniques in Python 3.8 using libraries such as Numpy [62], Pandas [63], and Scipy [64]. Below, we delineate all the feature engineering techniques experimented with in our study.

4.3.1. Raw spectral data

We had directly used the raw readings of all five chosen m/z ranges within the spectra, which resulted in 12,600 features (the combined bandwidth of all five biomarker ranges) for each sample. However, this could potentially overfit the ML models. Therefore, preprocessing methods can help to compress the feature space and prevent overfitting.

4.3.2. Statistical features

We calculated simple statistical features for each biomarker range, such as minimum, maximum, standard deviation, variance, skewness, kurtosis, and the number of peaks. Therefore, since we have five biomarkers and seven features, we generated a total of $5 * 7 = 35$ features. The statistical features extract the variables from the raw data and encapsulate the data in fewer dimensions, which reduces the burden on ML algorithms to learn patterns from the data.

4.3.3. Area under the curve (AUC)

As discussed in Section 4.2, the presence of a viral or human protein can be measured by the intensity of the spectral peak over a narrow distribution of m/z values and cannot be localized to a single point. Hence, AUC [65] is more suitable over local maxima for representing an effective viral or human protein signal as it aggregates the intensities of all points in the range. Moreover, Chivte et al. [13] established AUC as a reliable feature for distinguishing COVID-19 positive and negative samples using gargle samples analyzed via mass spectrometry. We use the biomarkers from Chivte et al. and describe them as B_0 – B_4 , as shown in Table 1.

4.3.4. Arithmetic combinations of the area under the curve values

Although the AUC captures the intensity of a biomarker, we observed a wide variance from one sample to another. This happens mainly due to two reasons. First, each sample has potentially different amounts of human/viral protein present, and second, information regarding exposure to the virus or the time course of infection was not possible to collect. Such differences in immune response and viral load would be reflected in the biomarker intensities. We tested different arithmetic combinations such as subtraction, addition, ratio, and product for each sample with all possible combinations of different biomarker pairs (shown in Table 2). Regardless, we observed that the ratio of AUC between pairs of biomarkers (listed in Table 2) showed a consistent pattern for positive and negative samples.

4.4. Data Preparation

We partitioned 152 samples from our MALDI-ToF dataset using a train-test-split strategy with a 70 : 30 train-test-split ratio to form two disjoint and independent splits. This minimizes data leakage from classifier training into calibration and performance assessment. Within the train and test splits, we kept the ratio of the count of positive to negative samples constant to maintain class balance. Our classifier uses the train-split dataset using features in Table 2 (containing 41 COVID-19 positive and 65 COVID-19 negative) and learns the COVID-19 prediction task. Then, we further calibrated the classifier using the same train-split dataset. Finally, we assessed the performance of the trained classifier on the unseen test-split dataset (containing 19 COVID-19 positive and 27 COVID-19 negative samples).

5. METHODS

We chose the random forest (RF) [59] classifier after assessing several machine learning algorithms and deep neural networks due to their superior performance. We observed that XGBoost had similar performance, however, random forests are easy to interpret, require less time to train, and are widely used in medicine paradigm [44, 34, 66]. The goal of the RF algorithm is to train a classifier function (f) that learns the relationships between the ratio features generated from training samples (x_{train}) and the outcome of the associated COVID-19 RT-PCR test (y_{train}). After training, we cal-

Feature	Description	Implication
R_0	AUC_{B_0} / AUC_{B_1}	HP1/HP2
R_1	AUC_{B_0} / AUC_{B_2}	HP1/VP1
R_2	AUC_{B_0} / AUC_{B_3}	HP1/VP2
R_3	AUC_{B_0} / AUC_{B_4}	HP1/HP3
R_4	AUC_{B_1} / AUC_{B_2}	HP2/VP1
R_5	AUC_{B_1} / AUC_{B_3}	HP2/VP2
R_6	AUC_{B_1} / AUC_{B_4}	HP2/HP3
R_7	AUC_{B_2} / AUC_{B_3}	VP1/VP2
R_8	AUC_{B_2} / AUC_{B_4}	VP1/HP3
R_9	AUC_{B_3} / AUC_{B_4}	VP2/HP3

Table 2

Ratio features generated from AUC values of five potential biomarkers.

ibrate the RF and test on new/unseen saliva samples (x_{test}) to evaluate the precision and recall metrics of the trained classifier's prediction ($f(x_{test}) = y_{test}$) as compared to the corresponding RT-PCR result. Further, we leverage the X-AI algorithms to illustrate explanations for the outcomes of the RF algorithm on both a global (all-samples) and local (per-sample) basis in a human-interpretable manner.

In this study, we have used several python libraries for implementing AI and X-AI algorithms. For instance, we used Scikit-Learn [67] for all machine learning algorithms and Tensorflow [68] for neural networks. Furthermore, for X-AI algorithms, we used Scikit-learn and SHAP library [69, 55].

5.1. Random Forest (RF) Classifier

RF is an ensemble classification algorithm that combines several tree predictors (Decision Trees [56]) to build a forest classifier. Each tree in the forest trains from a randomly sampled vector from the input features. These random vectors are sampled independently from the same distribution in the predictor space [59]. The outcome of a trained forest is the majority vote taken in as the mean or median of the predictions from all the independently trained trees. Additionally, in the RF algorithm, we can fine-tune the parameters such as the number of trees (also known as estimators) in the forest, methods of bootstrapping, and the properties of trees. If bootstrapping is enabled, random samples are drawn from the training set with replacements to train decision trees and take the majority vote. Furthermore, we can tune the core properties of each decision tree, such as maximum depth, the maximum number of leaves, splitting criterion, minimum samples per split, and minimum samples per leaf to optimize the performance.

Our first step in training the RF classifier was to find optimized hyperparameters by leveraging a randomized grid search technique with 5-fold cross-validation on the training dataset. Randomized search randomly picks hyperparameter configurations from our defined grid of hyperparameters, wherein we cataloged each configuration with its cross-validation accuracy score. Finally, the hyperparameter configuration with the best score (shown in Table 3) was selected

Hyperparameter	Value
Number of estimators	100
Bootstrap	True
Splitting criterion	Gini impurity
Maximum depth of tree	3
Minimum samples per split	2
Minimum samples per leaf	1

Table 3

Hyperparameters of our RF classifier.

to train the RF algorithm on complete training data, which is further evaluated and interpreted with the test-split data.

5.2. Random Forest Calibration

Our trained RF presents the output of a sample as a function of probability. The final outcome is then predicted as the class with the highest probability. If the trained RF model (f) computes the probability (P) for a sample (x_i) to test positive, then $P(f(x_i) == \text{COVID-19 positive})$ is computed as the fraction of trees in the forest that vote for COVID-19 positive. These probabilities can help medical practitioners to understand the certainty of having the disease for a COVID-19 diagnosis. Furthermore, the binary outcome of positive/negative tests does not help diagnose early infection and recovery stages. Rather than a simple “yes” or “no” answer, knowing the probability of having COVID-19 is crucial as it helps to understand the intermediary stages in the disease cycle.

Although RF achieves good performance, the predicted probabilities are sometimes out of step with their actual probabilities (i.e., the ratio of positive samples and the entire dataset). A classifier indicates ideal calibration if the predicted and actual probabilities are synchronized for the entire probability range 0 – 1 (shown as a gray dotted line in Figure 2). For example, if an ideally calibrated classifier predicts 0.8 probability for COVID-19 positive, then eight of ten samples should be COVID-19 positive (meaning actual probability is $8/10 = 0.8$). However, in a real-life scenario, the classifiers require additional calibration to refine their probability scores.

The most common calibration methods include isotonic regression [70] and Platt scaling [71]. Isotonic regression fits a step-wise regression function to the predicted probabilities and maps them to the actual probabilities, which usually works well for larger datasets. On the other hand, Platt scaling [71] is compatible with even smaller datasets such as ours. Platt scaling adds a one-dimensional logistic regression function to the output of RF that calibrates RF's predicted probabilities with a sigmoid function.

After calibrating RF, we investigated the quality of calibration by plotting a calibration curve (as shown in Figure 2) using the train-split dataset. The calibration curve has predicted probabilities (on the x-axis) and actual probabilities (on the y-axis). Note that the probabilities were binned into seven bins to make the curve less noisy and more readable. We observed that the probabilities were well-calibrated for

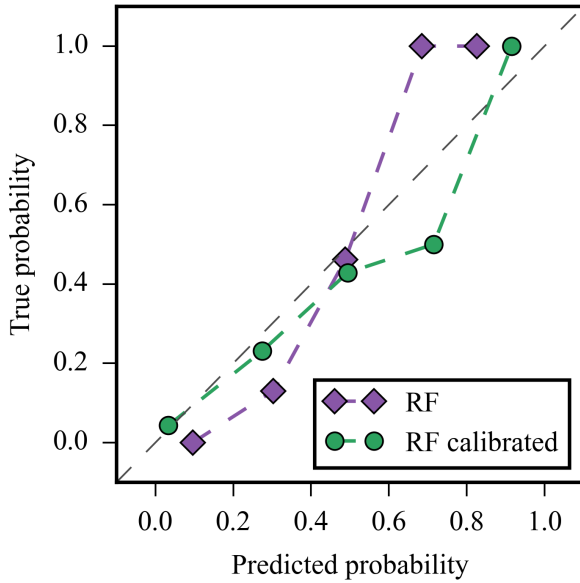


Figure 2: Calibration curves for un-calibrated and calibrated RF classifier. The gray dotted line represents an ideally calibrated classifier.

$P(f(x_i) == \text{COVID-19 positive}) (P)$	Positive	Negative	Total
$1 \geq P > 0.65$	45	2	47
$0.65 \geq P > 0.5$	3	7	10
$0.5 \geq P > 0.25$	7	15	22
$0.25 \geq P \geq 0$	5	68	73

Table 4

Samples in each region segregated with thresholds on probability (for calibrated classifier).

calibrated RF compared to the original RF. We also graphed the predicted probabilities for each sample in the train-split and the test-split datasets in Figure 3 to get a more in-depth view of the probability scores for each sample. According to the train-split dataset's probability scores, we found that setting a gatekeeper threshold for probability resulted in better performance. Hence, based on the train-split dataset, we set the threshold to predict COVID-19 positive as when probability (P) is $1 \geq P > 0.65$ and $0.25 \geq P \geq 0$ for COVID-19 negative. After setting the gatekeeper thresholds, we achieved 94.04% accuracy on the train-split dataset. Therefore, we used these thresholds on both train-split and test-split datasets and tabulated the count of positives and negatives in each threshold in Table 4. Using the thresholds on calibrated RF, overall, there were no false negatives and only two false positives across all samples. The false positives could be an experimental error in sample preparation or from the PCR analysis ground truth.

5.3. Random Forest Interpretation Using Explainable-AI

To instill trust in the model's predictions, we interpret the RF model both globally and locally using X-AI techniques. While global interpretation explains the importance of each feature in overall model prediction, local interpretation provides reasoning on a single instance level. For global interpretation, analyzing the importance of features determined by a trained model gives information about its prediction process. In this section, we leverage multiple techniques to investigate the feature importance of our trained RF model.

5.3.1. Impurity-based feature importance (IFI)

First, we interpreted the trained RF classifier with a model-specific IFI technique. This technique computes the feature importance as the average decrease in Gini impurity [72] from a feature node to its child nodes. Generally, except for the leaf nodes at the bottom of the tree, all other nodes have a threshold condition placed on a feature whose decision splits the node into two child nodes. The drop in impurity in this split is then calculated as the difference of Gini impurity between the node and the sum of its child nodes, weighted by the number of samples in each node. The final feature importance is the mean of drop in impurity at every prevailing feature node across the forest. Following these procedures, we calculated the IFI for all 10 features as shown in panel A of Figure 4 with the drop in Gini impurity on the y-axis and features on the x-axis. Although this method gives a general understanding of feature rankings, one disadvantage is the inflation of importance for features with high cardinality in the forest. Therefore, we investigated other feature-importance algorithms to validate the results.

5.3.2. Permutation Feature Importance (PFI)

The PFI technique [59] calculates the drop in performance when the trained RF algorithm is validated with permuted feature values which essentially makes the feature a noise. This method analyzes one feature at a time by permuting their values to break the association between the feature and the outcome. Clearly, the permutation of important features results in a larger performance drop. Therefore, the feature importance of using PFI is the drop in permuted feature accuracy from the base accuracy (where every feature was used in its original form). Bias from random value assignment to feature values was prevented by permuting values and averaging the drop in accuracy across 100 iterations. However, this algorithm fails to capture feature interaction effects as it permutes only one feature at a time. Panel B in Figure 4 shows the permutation importance scores for the RF classifier with overall feature importance printed on the y-axis and the features on the x-axis.

5.3.3. Shapely Additive Explanations (SHAP)

Lundberg and Lee [69] formalized the SHAP algorithm as an additive feature attribution technique that unifies concepts from local model-agnostic explanations (LIME) [73] and Shapely values [74]. In general, linear models are easy to interpret as the feature importance of the model is re-

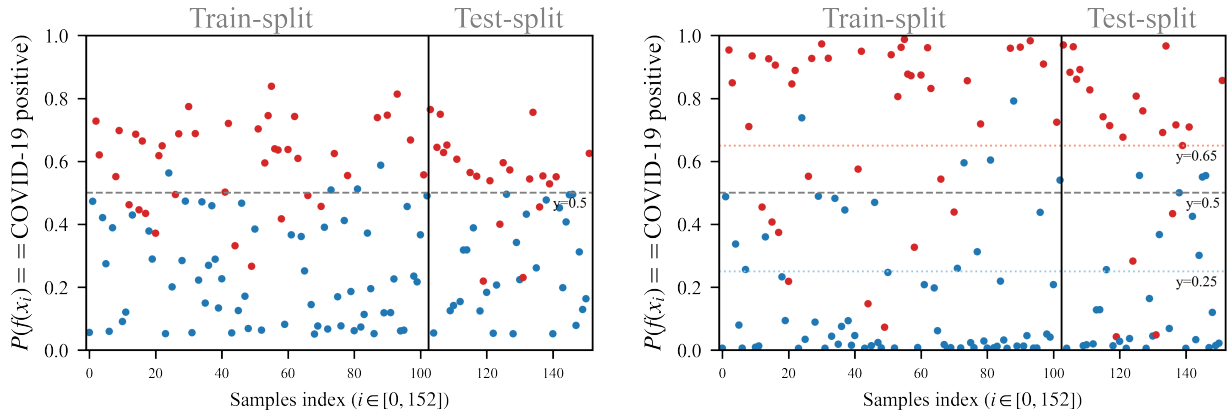


Figure 3: Probability of each sample (on the x-axis) to test COVID-19 positive (on the y-axis) for un-calibrated RF (on the left) and calibrated RF (on the right). The true labels for each sample are color-coded in blue and red for COVID-19 negative and positive tests respectively.

flected by the model's coefficients. However, due to the complexity of the RF algorithm, it cannot be interpreted as a simple linear model. The output of a single sample from RF, on the other hand, could be explained by producing some neighboring samples and then fitting a linear model locally on the newly obtained neighborhood samples. The LIME algorithm follows this approach: it generates a local point of view per sample by applying perturbations to its feature values and generating some artificial data in the neighborhood of a sample. LIME then fits a surrogate model on the artificial data and presents the coefficients of the surrogate model as the model interpretation. The downside of LIME is that it generates artificial samples using a heuristic kernel function. However, artificially replicating clinical data is difficult, and the dependence on kernel function heuristics to generate artificial samples is unreliable. SHAP adopts LIME procedures and bridges its limitations with the Shapely values, which borrow principles from cooperative game theory. Shapely values rationalize the distribution of credit or payoff among the players in a cooperative game by inspecting each player's contribution individually and collaboratively as a team [74].

In theory, the feature attributions assigned by our trained RF classifier (f) to the features R_i (where $i \in (0, 9)$ for 10 ratio features) in a given data sample (x) is computed as $(\phi_{R_i}(f, x))$ using Equation (3). This equation facilitates SHAP to compute a unique optimal solution for feature attribution by combining individual as well as team efforts. This can be understood in light of PFI, where we extracted feature attributions by masking each feature at a time and computing the drop in performance of the classifier. PFI captures individual contributions but fails to grasp collaborative contributions. The more intuitive approach of SHAP allows for collaborative contributions in conjunction with individual contributions to be considered by iterating over all possible subsets S in our feature space having F number of features excluding feature R_i (where $F = 10$) as $S \subseteq F/\{R_i\}$. In each subset, the marginal contribution (C) of feature R_i is

extracted as the difference in the outcome of the function f with and without R_i in the subset as shown in Equation (1) where $f_{S \cup \{R_i\}}$ and f_S are two retrained functions with and without R_i respectively that are marginalized over features absent in the subset. The resultant sum of C is weighted with W (refer to Equation (2)) whose numerator is the product of the different number of ways a subset can be formed ($S!$) and the number of ways to choose features excluding the features in a subset $((|F| - |S| - 1)!)!$. The numerator is normalized by $F!$, the total possible ways of choosing the features. Finally, for each feature in x , Equation 3 computes the SHAP values through iterations over all possible subsets S . The magnitude of final SHAP values shows the contribution of a feature to the outcome of the classifier. In this sense, the positive or negative SHAP value indicates the feature's support towards the COVID-19 positive or negative decision respectively.

$$C = f_{S \cup \{R_i\}}(x_{S \cup \{R_i\}}) - f_S(x_S) \quad (1)$$

$$W = \frac{|S|!(|F| - |S| - 1)!}{|F|!} \quad (2)$$

$$\phi_{R_i}(f, x) = \sum_{S \subseteq F/\{R_i\}} W \times C \quad (3)$$

Since the idea behind Shapely values is that there exists only one solution to allocate the attributions, the results are more reliable than previous methods such as LIME [73]. In addition to this, SHAP has other desirable axiomatic properties. The local accuracy property entails that the sum of all feature attributions of a model should approximate the original model meaning $f(x) = \phi_{R_n} + \sum_{i=0}^9 \phi_{R_i}$, where R_n is the feature attribution when all features are toggled off.

The missingness property ensures that the features toggled off have no impact on the model's output. Lastly, the consistency property ensures for any feature R_i , ϕ_{R_i} remains consistent with respect to the impact of feature values of any retrained model. For example, in two functions (f_1, f_2) trained on different subsets including the feature R_i , if the feature values of R_i have larger impact on f_1 than f_2 , then $\phi_{R_i}(f_1, x) \geq \phi_{R_i}(f_2, x)$.

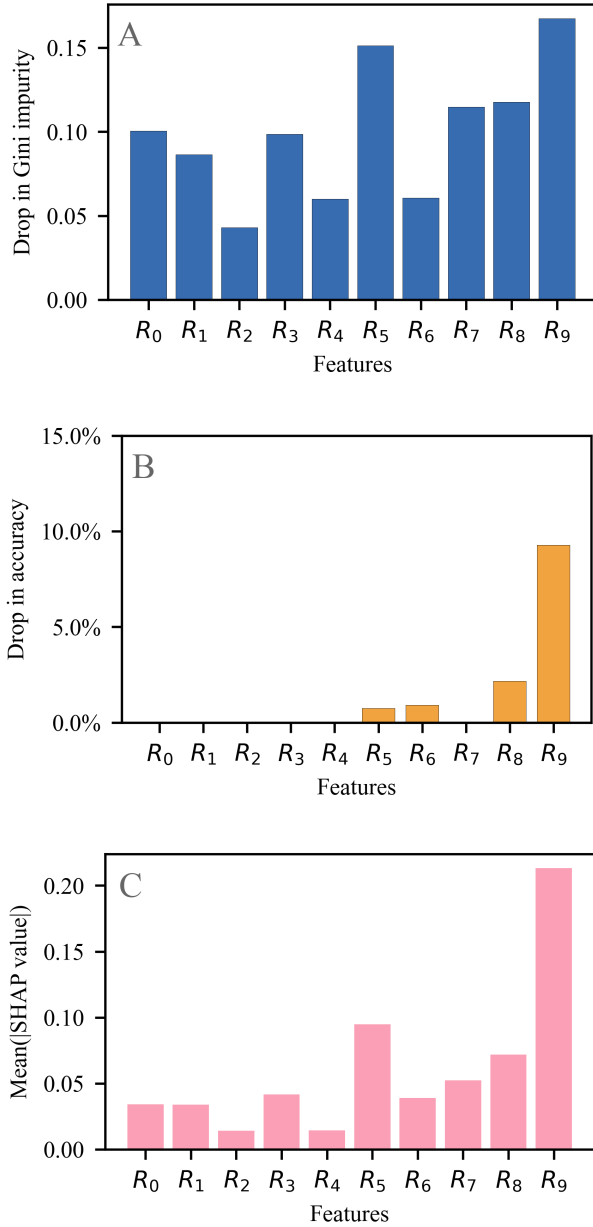


Figure 4: Feature importance for RF classifier using three feature interpretation techniques: Impurity-based feature importance (panel A, top), Permutation Feature Importance (panel B, middle), and Shapely Additive Explanations (panel C, bottom). The y-axis shows the feature importance for each feature shown on the x-axis.

We then combine Equations (1), (2), and (3) and com-

pute SHAP values for 46 testing samples having 10 ratio features. The result is a SHAP value matrix of dimensions $[46 \times 10]$ that will aid in the local and global model interpretation of our trained RF model. For global model interpretation, we extract the magnitude of feature importances in two steps: 1) take the absolute SHAP values, which nullify the effect of direction, and 2) compute the mean of absolute SHAP values across all samples. This results in condensing the $[46 \times 10]$ matrix to a single array of 10 feature importances (as shown in panel C of Figure 4). By comparing all 3 feature importance algorithms in Table 5, it is conclusive that the two most important features are R_9 and R_5 , and the least important are R_2 and R_4 . In addition to global (all-sample) explanations, we present local (per-sample) explanations using the SHAP value matrix as shown in Figure 8. The x-axis represents the SHAP value per sample, and features are numbered on the y-axis. We encoded the feature values in color ranging from blue (signifying small value) to red (signifying large value) and assigned each feature to a quartile based on its value as shown at the origin of each bar. The magnitude of each bar explains the impact of each feature on the model's output and thus allowing us to interpret them as feature importance. We provide more details on global and local explanations in sections 6.2.1 and 6.2.2, respectively.

6. Results

6.1. Results of Random Forest Classifier

We trained the RF algorithm with the hyperparameters (shown in Table 3) extracted through an exhaustive grid search. Then, we employed a total of 106 samples in training and 46 in testing the model. Then we calibrated the trained RF algorithm using Platt scaling and set a threshold on predicted probability for COVID-19 diagnosis at 0.65 and 0.25 for COVID-19 positive and COVID-19 negative diagnosis. The thresholds' rationale is that samples on the border of diagnosis (i.e., probability == 0.5) may require special attention or re-testing. Secondly, in Figure 3, we observed that the confidence samples between the thresholds of 0.65 and 0.25 are lower, which is undesirable in real-time conditions. All in all, 21% of samples had low confidence, and the remaining 79% had high confidence with 94.44% accuracy on the test-split and 94.04% accuracy on the train-split. Similar high accuracies on training and test sets ensure that the model is not overfitted. We also show a confusion matrix for both splits in Figure 5. Overall, only 2 and 5 samples are classified falsely in the test and train datasets, respectively. As mentioned earlier, our dataset had more negative samples than positive ones, making it crucial to examine the model's accuracy for both positive and negative categories. Therefore, we evaluated precision, recall, and F1 metrics on both the test and train datasets for positive and negative samples independently. As shown in the evaluation report (in Figure 6), the train-split had a high precision, recall, and F1-score of 0.96, 0.94, 0.95 for the COVID-19 negative samples and 0.91, 0.94, 0.92 for positive samples, respectively. On the

Method	Order of feature importances
Impurity-based feature importance	$R_9 > R_5 > R_8 > R_7 > R_0 > R_3 > R_1 > R_6 > R_4 > R_2$
Permutation feature importance	$R_9 > R_8 > R_6 > R_5 = R_0 = R_7 = R_1 = R_3 = R_4 = R_2$
Shapely additive explanations	$R_9 > R_5 > R_8 > R_7 > R_3 > R_6 > R_0 > R_1 > R_4 > R_2$

Table 5

Global feature importances shown in descending order for different feature interpretation techniques.

other hand, precision, recall, and F1-scores for COVID-19 negative and positive for the test-split were 1.00, 0.90, 0.95 and 0.88, 1.00, 0.94, respectively. In the case of test-split, there were 0 false positives, 2 false negatives, and 34 true predictions. In train-split, the false predictions were slightly higher with 2 false positives and 3 false negatives and a total of 79 correct predictions. Although these metrics portray the high efficiency of the trained model in COVID-19 testing, it still does not provide a means to understand its prediction mechanisms. This motivated us to dissect the trained RF model further and understand its prediction mechanisms using X-AI techniques.

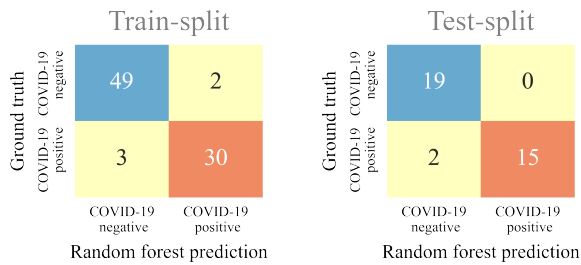


Figure 5: Confusion matrices for the RF classifier on the train-split and test-split datasets.

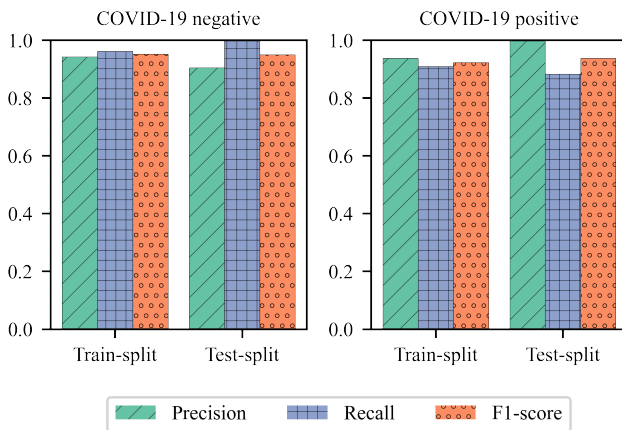


Figure 6: Precision, recall and F1-score dataset for COVID-19 negative (on left) and COVID-19 positive (on right) shown for train-, and test-splits for the un-calibrated classifier (on top) and calibrated classifier (on bottom).

6.2. Model Interpretation of Random Forest Classifier

The outcome of the RF model is more complex than a simple decision tree. In decision trees, we have a single decision path for each prediction which makes the model self-interpretable. However, RF coalesces the outcome of many unique decision trees, meaning for each sample, there is a multitude of decision paths; one for each tree traversal which makes model interpretation complex. Therefore, we simplify the interpretation of RF by presenting the rationale behind predictions in the form of global (all sample basis) and local (per sample basis) interpretations. These interpretations help domain experts and clinicians handling COVID-19 testing to understand the operations of the classifier and gain rich diagnostic information. First, the idea of the global interpretation of a model goes beyond the analysis of feature importance. It can elaborate on how the distribution of each feature affects the model prediction. Second, local interpretation operates on one sample at a time and delineates each feature's value and contribution to the outcome of RF.

6.2.1. Global Interpretation

As shown earlier, each of the three feature importance algorithms found similar feature ranking: R_9 , R_5 , and R_8 were consistent among the top four features while the bottom two were R_2 and R_4 (Table 5). It is fairly common to observe slight differences in the feature importance across the three algorithms due to underlying procedural differences and the shortcomings of techniques highlighted in their respective sections. However, on the whole, these rankings reveal that most feature importances assigned by the three algorithms are fairly consistent. The consistent nature of feature attribution shows that our RF algorithm can be understood when viewed from different perspectives of the X-AI algorithms. Although these are important findings, they do not explain how the model prediction correlates with the feature values. While IFI and PFI algorithms can generate feature rankings, they do not provide enough information to explore the interactions between features. Therefore, we extended our X-AI approach to the SHAP algorithm, which can analyze feature interactions, data distribution, and the model's dependency on it.

The SHAP algorithm generated a violin plot, which provides a fine-grained view of SHAP values (feature importance) and feature value distribution as shown in Figure 7. This plot illustrates the trends of SHAP values in conjunction with feature values by plotting the SHAP value matrix

(as described in section 5.3.3) without aggregation across all test-split samples. In addition, the plot encodes the density of the samples have a certain SHAP value as the width of the line. To interpret these plots, the higher the SHAP value, the greater the importance; the positive SHAP values support positive COVID-19 prediction, negative values support negative output; and the feature value's are represented on a blue-red color-bar where deep blue and deep red correspond to low and high feature values. For example, the feature R_9 has SHAP values extending up to +0.475 towards a positive COVID-19 decision, where the feature value is low. For a negative test, mostly high values of R_9 contributed towards a negative COVID-19 prediction. On the contrary, for feature R_5 , lower and higher feature values contribute towards COVID-19 negative and positive tests, respectively. Features R_6 and R_7 follow similar patterns as R_5 while R_0 and R_1 have similar patterns of R_9 .

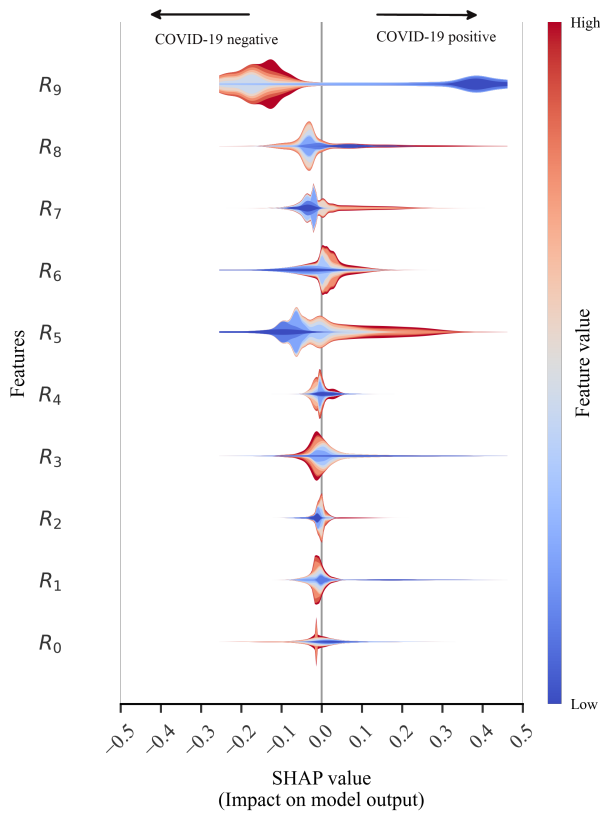


Figure 7: Violin plot for global interpretation of calibrated RF classifier using SHAP values.

The violin plot provides an approximate idea about the model output for any sample based on the feature distribution. This can be immensely helpful to cross-examine the model if the model prediction is not following the trend of the violin plot. For example, if the model is predicting COVID-19 positive for a sample where the R_9 feature value is very high, we can easily identify that the model is not following the trend, and hence, it needs further validation. It also shows any outliers in the dataset, for instance, higher feature values of R_8 colored in deep red color have a large SHAP

value. However, the width of the line is very thin which indicates that the number of samples is potentially very less or could be just the case of one outlier. This kind of information is critical to instill trust in users as it allows them to question outputs from the model.

6.2.2. Local Interpretation

We provide the local interpretation of the RF classifier with a holistic view of the classifier's performance by viewing different cases in prediction, such as a true positive (TP), a false positive (FP), a true negative (TN), and a false negative (FN) (as shown in Figure 8 and Table 6). Each bar in Figure 8 is colored using a color bar encoded with deep blue and deep red, corresponding to the lowest and highest feature value. Lastly, the feature importance, similar to the global SHAP plots, is shown on the x-axis, where a positive value indicates support for COVID-19 positive and COVID-19 negative otherwise.

The local interpretation helps us understand how, for any individual sample, different features interact to sway the RF model's final decision. We first analyze a true positive prediction by RF, with probability, $P = 0.964$ (in panel A of Figure 8). In panel A, R_9 and R_5 have the largest positive SHAP value and hence show strong support for a COVID-19 positive outcome, followed by R_8 , R_4 , R_2 and R_1 with a lower positive SHAP value. Although R_0 , R_3 , and R_7 support a negative outcome (with a negative SHAP value) in the true positive sample (panel A), other features provide overall stronger support for a positive outcome, which outweighs support for a negative outcome. In the true negative record with $P = 0.045$ (shown in panel D of Figure 8), all features marginally support a negative outcome, and no features support a positive outcome. Moving to panels B and E, we show two cases with low confidence in the prediction for COVID-19 positive and negative (i.e., the probability is close to 0.5). Again, panel B is a true positive prediction similar to panel A; however, panel B has lower confidence in the prediction with a predicted probability of $P = 0.691$. The reason could be explained by inspecting the SHAP values. First, features R_9 and R_8 have low and high SHAP values, which show an inversion from panel A. Second, R_0 in panel B has a higher SHAP value than panel A. On the other, in panel E, R_8 , R_7 , R_4 , R_3 , and R_1 support a positive decision, while others support a negative decision resulting in less confidence in the final outcome (i.e., prediction probability, $P = 0.425$). Finally, we show a false positive (panel C) with $P = 0.55$ and a false negative (panel F) with $P = 0.283$. In case of a false positive, only R_6 , R_1 , and R_0 sway the decision towards negative prediction while all other features strongly support a COVID-19 positive outcome. Similarly, for the false negative in panel F, R_7 , R_6 , and R_5 support a positive outcome and all other features point towards a negative outcome. In both false predictions, we can visually observe a large discrepancy among each feature's support for the COVID-19 outcome.

In addition to SHAP values, the feature values can be used to understand different patterns between feature val-

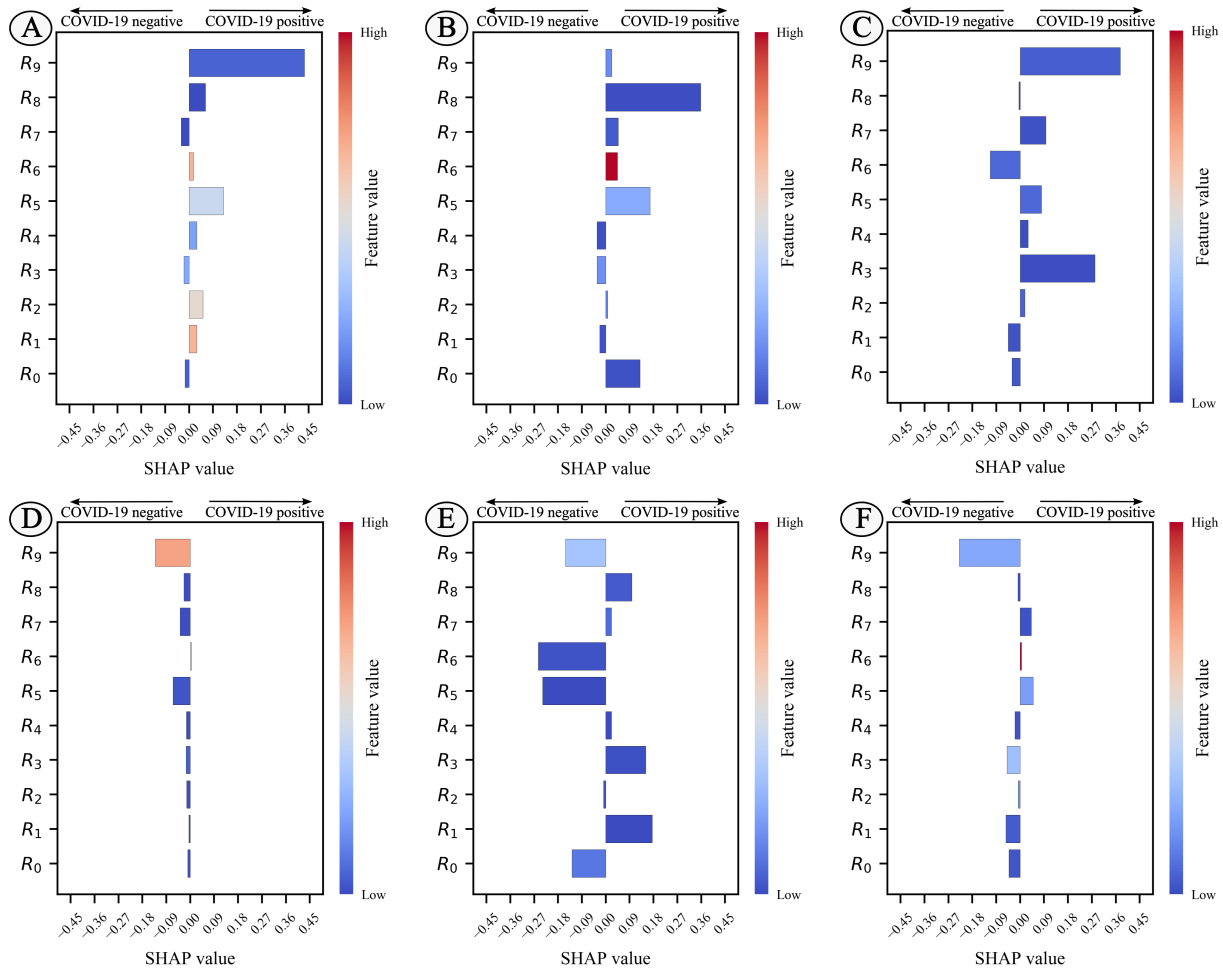


Figure 8: Local explanations generated using SHAP algorithm for six records for COVID-19 positive predictions (panels A, B, and C) and COVID-19 negative predictions (panels D, E, and F). Panels A and D show highly confident predictions, panels B and E show low confident predictions, and panels C and F show false positive and false negative predictions, respectively.

Index	True label	Stage-1	Stage-2	Stage-3			Stage-4
		Model prediction	Inspect probability	Turn to local interpretation			Final decision
				Check-1	Check-2	Check-3	
Panel-A	Positive	Positive	0.964	✓	✓	✓	Valid test
Panel-B	Positive	Positive	0.691	✓	✓	✓	Valid test
Panel-F	Positive	Negative	0.283	✓	✗	✗	Requires further inspection
Panel-D	Negative	Negative	0.045	✓	✓	✓	Valid test
Panel-E	Negative	Negative	0.425	✗	✗	✗	Requires further inspection
Panel-C	Negative	Positive	0.55	✗	✗	✗	Requires further inspection

- **Check-1** Are some or all of the most features in the global interpretation (e.g., R_9 , R_8 , R_7 , and R_5) are also important in the local interpretation?
- **Check-2** Is there is any disagreement between the most important features support for COVID-19 positive and negative prediction?
- **Check-3** Do all the important values fall into the dense regions of Figure 7, with no outliers?

Table 6

An explainable-AI framework for COVID-19 diagnosis decision making.

ues and their impact on a COVID-19 positive or negative decision. After analyzing several local interpretation plots, we found that the feature value was easier to interpret using color bars than discrete feature values. Therefore, we infer the feature values as low range (deep blue), high-range (deep red), and mid-range (between deep blue and deep red). The feature values help us see how each sample compares against the rest of the samples in the dataset with the aid of global interpretations in Figure 7. For instance, the feature R_9 in panels A and C is deep blue, indicating a feature value closer to the lowest value observed in our dataset. Now, analyzing the feature values with respect to Figure 7, the distribution of feature values at the lower end and higher end of the spectrum are relatively dense compared to the mid-region. As discussed in Section 6.2.1, the density of samples in the dataset at any given SHAP value can be realized by the width of the marker in violin plot. This shows that the R_9 feature follows a similar trend as the majority of samples in the dataset. In panels A and C, the features with the next largest SHAP value after R_9 are R_5 , R_6 , and R_3 . These three features fall in the mid-range in panel A, whereas panel C has feature values at the lower end. From the violin plot, we can see again that the lowest feature values for R_3 , R_5 , and R_6 have a thin line that highlights that feature value is a minority in the dataset or could potentially be an outlier. Such analysis would benefit a medical practitioner in charge of making decisions about the COVID-19 test outcome with a local analysis and inspection of the features that contributed most towards a positive or negative test. This, in conjunction with consideration of a patient's symptoms, can lead to more informed conclusions and diagnoses.

We provide a summary of our entire framework from RF prediction to making final decision in four stages as described in Table 6. First, in Stage-1, we get the binary prediction from RF model if a given sample is COVID-19 positive or negative test. Next, we move to Stage-2 where we assess the probability for prediction and check if the probability is within the gatekeeper threshold; $1 \geq P > 0.65$ for COVID-19 positive and $0.25 \geq P \geq 0$ for COVID-19 negative. After assessing probabilities, in Stage-3, we turn to local model interpretations, where we framed three key points to check to assess the validity of the test. Briefly, Check-1 sees if the most important features (i.e., R_9 , R_8 , R_7 , and R_5) are also important in local interpretation. Next, we pass Check-2 if the most important features support either a COVID-19 positive or negative outcome. Finally, in Check-3, we examine the feature values by comparing them to the global interpretation plot and mark any outliers as we discussed in the above examples. A valid case would ideally answer yes to all three checks. However, if any one of the check fails, it would mean that the test is invalid. We present these conclusions in Stage-4 as a valid test or if it requires further inspection.

7. Discussion

While analyzing our results through different interpretation techniques, we observed quite remarkably that all three

methods of global feature interpretation consistently resulted in the most important features as R_9 and R_5 (Table 5). The meaning of these features is of particular interest because of the biomarker ranges making up the features, AUC_{B_3}/AUC_{B_4} for R_9 and AUC_{B_1}/AUC_{B_3} for R_5 . First, the features R_9 and R_5 are host-to-virus and virus-to-host features, respectively, representing the interaction between host immune response and viral antigen, as described in [13]. Second, the viral protein fragment corresponding to B_3 is tentatively suggested to be the S1 subunit of the viral spike protein (see Table 1). S1 is a key viral biomarker in the mass spectra because the observed m/z ratio does not overlap significantly with other proteins or fragments from the gargle sample.

The least important features, R_4 and R_2 , were decidedly the same by each method. R_4 contains B_2 , which is ambiguous in that the AUC value for this peak may consist of *both* human and viral proteins (for example, a small amount of human serum albumin and spike protein S2 subunit (B_2), respectively). Therefore, the presence of B_2 could render R_4 less important, as B_2 would be present in both disease and non-disease states. Considering the nature of the biomarkers, it was odd that R_2 was not found to be as important as R_5 , as both ratio features should technically represent the same proteins, as B_0 represents the AUC of the double charged ion of B_1 . To investigate this, the correlation plot between each ratio feature value was plotted, and not surprisingly, R_5 and R_2 showed a positive Pearson correlation of 0.62. This is most likely why R_2 was deemed less important than R_5 and the least important feature since RF avoids repetitive predictions by not placing importance on features equivalent in meaning. It should be noted once again that each biomarker has been assigned a putative identity based on preliminary studies only and have yet to be unambiguously characterized.

Turning to local feature interpretations, these could offer a powerful, comprehensive diagnostic view in contrast to a binary decision by RT-PCR or an algorithm with percent confidence. The local explanations generated using SHAP values show the contribution of each feature in each sample. This could allow domain experts and health officials administering such a test to make more informed decisions based on the putative host-to-viral or viral-to-host ratios for case-by-case bases, as seen in Figure 8. If the algorithm decides positive or negative, the local feature explanation will provide additional information as to *why* the test output its decision. Although data augmentation techniques could enrich the dataset with more artificial samples, we avoided doing this because it could have made the dataset noisy by adding false patterns. Nonetheless, not only in this diagnostic approach is the viral aspect of COVID-19 considered (as is only considered in PCR-based tests), but the human immune response towards the COVID-19 virus is also given due consideration. This results showed that machine learning algorithms (e.g., RF) coupled with the utility of X-AI interpretability could be implemented into healthcare to address the limitations of black box systems and improve the diagnostic process, from test output to informed care.

In summary, from training machine learning algorithms to explaining the trained models, each aspect may be of particular interest for different reasons. For example, during the AI-model building stages, a closer view of calibration, probabilities, confusion matrices, precision, and recall values for the training and testing datasets can prevent overfitting and bias. Following that, the interpretation of a model on a global and local level can have several applications. First, from a machine learning perspective, feature importance can help identify spurious correlations between features and diagnoses and monitor model drift. Second, biochemistry researchers can learn and investigate the relationships between feature value to its importance in the outcome of COVID-19 diagnosis. Finally, in a clinical setting, the local model interpretations, along with the probability scores, can aid in determining whether a test was properly executed or if a follow-up test was required.

8. Conclusion

In this work, we have designed an AI-based COVID-19 diagnostic method using the MALDI-ToF MS protein profiles of human gargle samples. After thoroughly validating various machine learning algorithms, we found the performance of random forest (RF) to be the best among others. We evaluated the RF classifier on a 70% – 30% train-test-split strategy where the accuracy on the test dataset was 94.44%. We further utilized the concepts of X-AI and interpreted the RF algorithm using SHAP and feature importance techniques such as permutation feature importance and impurity-based feature importance to find the most important features. Using these interpretation models, we showed global and local explanations of the model's decision on COVID testing. Explaining the rationale behind the decision makes our approach trustworthy by enabling domain experts and medical practitioners to understand the mechanisms of the black-box AI models when used on a real-time basis. Additionally, this methodology may allow for more detailed information about the life cycle of viral infection along with the COVID-19 status ascertained from the MALDI-MS data.

Declaration of competing interest

The authors declare that there is no conflict of interest regarding the publication of the article.

References

- [1] World Health Organization (WHO), WHO COVID-19 Dashboard, 2022. URL: <https://covid19.who.int/>.
- [2] C. Sohrabi, Z. Alsafi, N. O'Neill, M. Khan, A. Kerwan, A. Al-Jabir, C. Iosifidis, R. Agha, World health organization declares global emergency: A review of the 2019 novel coronavirus (COVID-19), *International Journal of Surgery* 76 (2020) 71–76.
- [3] National Center for Immunization and Respiratory Diseases (NCIRD), Division of Viral Diseases, SARS-CoV-2 variant classifications and definitions, 2022. URL: <https://www.cdc.gov/coronavirus/2019-ncov/variants/variant-info.html>.
- [4] M. Nicola, C. Sohrabi, G. Mathew, A. Kerwan, A. Al-Jabir, M. Griffin, M. Agha, R. Agha, Health policy and leadership models during the COVID-19 pandemic-review article, *International Journal of Surgery* 81 (2020) 122–129.
- [5] P. Habibzadeh, M. Mofatteh, M. Silawi, S. Ghavami, M. A. Faghihi, Molecular diagnostic assays for COVID-19: an overview, *Critical Reviews in Clinical Laboratory Sciences* 58 (2021) 385–398.
- [6] L. J. Carter, L. V. Garner, J. W. Smoot, Y. Li, Q. Zhou, C. J. Saveson, J. M. Sasso, A. C. Gregg, D. J. Soares, T. R. Beskid, S. R. Jervey, C. Liu, Assay techniques and test development for COVID-19 diagnosis, *ACS Central Science* 6 (2020) 591–605.
- [7] W. Feng, A. M. Newbigging, C. Le, B. Pang, H. Peng, Y. Cao, J. Wu, G. Abbas, J. Song, D.-B. Wang, et al., Molecular diagnosis of COVID-19: challenges and research needs, *Analytical chemistry* 92 (2020) 10196–10209.
- [8] P. Lasserre, B. Balansethupathy, V. J. Vezza, A. Butterworth, A. Macdonald, E. O. Blair, L. McAteer, S. Hannah, A. C. Ward, P. A. Hoskisson, et al., Sars-cov-2 aptasensors based on electrochemical impedance spectroscopy and low-cost gold electrode substrates, *Analytical chemistry* 94 (2022) 2126–2133.
- [9] E. Valera, A. Jankelow, J. Lim, V. Kindratenko, A. Ganguli, K. White, J. Kumar, R. Bashir, COVID-19 point-of-care diagnostics: present and future, *ACS Nano* 15 (2021) 7899–7906.
- [10] I. Sivanesan, J. Gopal, R. S. Vinay, L. E. Hanna, J.-W. Oh, M. Muthu, Consolidating the potency of matrix-assisted laser desorption/ionization-time of flight mass spectrometry (MALDI-TOF MS) in viral diagnosis: extrapolating its applicability for COVID diagnosis?, *TrAC Trends in Analytical Chemistry* 150 (2022) 116569.
- [11] M. Preianò, S. Correnti, C. Pelaia, R. Savino, R. Terracciano, Maldi MS-based investigations for SARS-CoV-2 detection, *BioChem* 1 (2021) 250–278.
- [12] M. Spick, H. M. Lewis, M. J. Wilde, C. Hopley, J. Huggett, M. J. Bailey, Systematic review with meta-analysis of diagnostic test accuracy for COVID-19 by mass spectrometry, *Metabolism* 126 (2022) 154922.
- [13] P. Chivte, Z. LaCasse, V. D. R. Seethi, P. Bharti, J. Bland, S. S. Kadkol, E. R. Gaillard, MALDI-ToF protein profiling as a potential rapid diagnostic platform for COVID-19, *Journal of Mass Spectrometry and Advances in the Clinical Lab* 21 (2021) 31–41.
- [14] M. Khan, M. T. Mehran, Z. U. Haq, Z. Ullah, S. R. Naqvi, M. Ihsan, H. Abbass, Applications of artificial intelligence in covid-19 pandemic: A comprehensive review, *Expert systems with applications* 185 (2021) 115695.
- [15] F. M. Nachtigall, A. Pereira, O. S. Trofymchuk, L. S. Santos, Detection of SARS-CoV-2 in nasal swabs using MALDI-MS, *Nature Biotechnology* 38 (2020) 1168–1173.
- [16] W. S. Noble, What is a support vector machine?, *Nature Biotechnology* 24 (2006) 1565–1567.
- [17] M. F. Rocca, J. C. Zintgraff, M. E. Dattero, L. S. Santos, M. Ledesma, C. Vay, M. Prieto, E. Benedetti, M. Avaro, M. Russo, et al., A combined approach of MALDI-ToF mass spectrometry and multivariate analysis as a potential tool for the detection of SARS-CoV-2 virus in nasopharyngeal swabs, *Journal of Virological Methods* 286 (2020) 113991.
- [18] N. K. Tran, T. Howard, R. Walsh, J. Pepper, J. Loegering, B. Phinney, M. R. Salemi, H. H. Rashidi, Novel application of automated machine learning with MALDI-ToF-MS for rapid high-throughput screening of COVID-19: a proof of concept, *Scientific Reports* 11 (2021) 1–10.
- [19] H. Rashidi, N. Tran, S. Albahra, Machine intelligence learning optimizer (MILO), "<https://milo-ml.com/>", 2022.
- [20] T. Chen, C. Guestrin, Xgboost: A scalable tree boosting system, *Proceedings of the 22nd ACM SIGKDD International Conference on Knowledge Discovery and Data Mining* (2016) 785–794.
- [21] Y. LeCun, Y. Bengio, G. Hinton, Deep learning, *Nature* 521 (2015) 436–444.
- [22] M. Deulofeu, E. García-Cuesta, E. M. Peña-Méndez, J. E. Conde, O. Jiménez-Romero, E. Verdú, M. T. Serrando, V. Salvadó, P. Boadas-Vaello, Detection of SARS-CoV-2 infection in human nasopharyngeal samples by combining MALDI-ToF-MS and artificial intelligence, *Frontiers in Medicine* 8 (2021) 398.

- [23] S. Wold, K. Esbensen, P. Geladi, Principal component analysis, *Chemometrics and Intelligent Laboratory Systems* 2 (1987) 37–52.
- [24] L. Yan, J. Yi, C. Huang, J. Zhang, S. Fu, Z. Li, Q. Lyu, Y. Xu, K. Wang, H. Yang, et al., Rapid detection of COVID-19 using MALDI-TOF-based serum peptidome profiling, *Analytical chemistry* 93 (2021) 4782–4787.
- [25] R. Tibshirani, Regression shrinkage and selection via the lasso, *Journal of the Royal Statistical Society: Series B (Methodological)* 58 (1996) 267–288.
- [26] L. Ståhle, S. Wold, Partial least squares analysis with cross-validation for the two-class problem: A Monte Carlo study, *Journal of Chemometrics* 1 (1987) 185–196.
- [27] I. Guyon, J. Weston, S. Barnhill, V. Vapnik, Gene selection for cancer classification using support vector machines, *Machine Learning* 46 (2002) 389–422.
- [28] M. M. Costa, H. Martin, B. Estellon, F.-X. Dupé, F. Saby, N. Benoit, H. Tissot-Dupont, M. Million, B. Pradines, S. Granjeaud, et al., Exploratory study on application of maldi-tof-ms to detect sars-cov-2 infection in human saliva, *Journal of Clinical Medicine* 11 (2022) 295.
- [29] Y. Benjamini, Y. Hochberg, Controlling the false discovery rate: a practical and powerful approach to multiple testing, *Journal of the Royal Statistical Society: Series B (Methodological)* 57 (1995) 289–300.
- [30] Z. Salahuddin, H. C. Woodruff, A. Chatterjee, P. Lambin, Transparency of deep neural networks for medical image analysis: A review of interpretability methods, *Computers in Biology and Medicine* 140 (2022) 105111.
- [31] H. Gong, M. Wang, H. Zhang, M. F. Elahe, M. Jin, An explainable ai approach for the rapid diagnosis of COVID-19 using ensemble learning algorithms, *Frontiers in Public Health* 10 (2022) 874455.
- [32] L. M. Thimoteo, M. M. Vellaco, J. Amaral, K. Figueiredo, C. L. Yokoyama, E. Marques, Explainable artificial intelligence for COVID-19 diagnosis through blood test variables, *Journal of Control, Automation and Electrical Systems* 33 (2022) 625–644.
- [33] M. Rostami, M. Oussalah, A novel explainable COVID-19 diagnosis method by integration of feature selection with random forest, *Informatics in Medicine Unlocked* 30 (2022) 100941.
- [34] M. A. Alves, G. Z. Castro, B. A. S. Oliveira, L. A. Ferreira, J. A. Ramirez, R. Silva, F. G. Guimarães, Explaining machine learning based diagnosis of covid-19 from routine blood tests with decision trees and criteria graphs, *Computers in Biology and Medicine* 132 (2021) 104335.
- [35] Q. Ye, J. Xia, G. Yang, Explainable ai for covid-19 ct classifiers: An initial comparison study, in: *2021 IEEE 34th International Symposium on Computer-Based Medical Systems (CBMS)*, IEEE, 2021, pp. 521–526.
- [36] F. Ullah, J. Moon, H. Naeem, S. Jabbar, Explainable artificial intelligence approach in combating real-time surveillance of covid19 pandemic from ct scan and x-ray images using ensemble model, *The Journal of Supercomputing* (2022) 1–26.
- [37] M. Pennisi, I. Kavasidis, C. Spampinato, V. Schinina, S. Palazzo, F. P. Salanitri, G. Bellitto, F. Rundo, M. Aldinucci, M. Cristofaro, et al., An explainable ai system for automated covid-19 assessment and lesion categorization from ct-scans, *Artificial intelligence in medicine* 118 (2021) 102114.
- [38] A. Basu, K. H. Sheikh, E. Cuevas, R. Sarkar, Covid-19 detection from ct scans using a two-stage framework, *Expert Systems with Applications* 193 (2022) 116377.
- [39] Q. Hu, F. N. B. Gois, R. Costa, L. Zhang, L. Yin, N. Magaia, V. H. C. de Albuquerque, Explainable artificial intelligence-based edge fuzzy images for covid-19 detection and identification, *Applied Soft Computing* 123 (2022) 108966.
- [40] N. Sharma, L. Saba, N. N. Khanna, M. K. Kalra, M. M. Fouda, J. S. Suri, Segmentation-based classification deep learning model embedded with explainable ai for covid-19 detection in chest x-ray scans, *Diagnostics* 12 (2022) 2132.
- [41] T. Ozturk, M. Talo, E. A. Yildirim, U. B. Baloglu, O. Yildirim, U. R. Acharya, Automated detection of covid-19 cases using deep neural networks with x-ray images, *Computers in biology and medicine* 121 (2020) 103792.
- [42] A. A. Ardakani, A. R. Kanafi, U. R. Acharya, N. Khadem, A. Mohammadi, Application of deep learning technique to manage covid-19 in routine clinical practice using ct images: Results of 10 convolutional neural networks, *Computers in biology and medicine* 121 (2020) 103795.
- [43] C. Wen, S. Liu, S. Liu, A. A. Heidari, M. Hijji, C. Zarco, K. Muhammad, Acns: Attention capsule sampling network for diagnosing covid-19 based on chest ct scans, *Computers in Biology and Medicine* (2022) 106338.
- [44] D. N. Vinod, B. R. Jeyavadhanam, A. M. Zungeru, S. Prabakaran, Fully automated unified prognosis of covid-19 chest x-ray/ct scan images using deep covix-net model, *Computers in Biology and Medicine* 136 (2021) 104729.
- [45] H. Li, N. Zeng, P. Wu, K. Clawson, Cov-net: A computer-aided diagnosis method for recognizing covid-19 from chest x-ray images via machine vision, *Expert Systems with Applications* 207 (2022) 118029.
- [46] M. A. Rahman, M. S. Hossain, N. A. Alrajeh, B. Gupta, A multi-modal, multimedia point-of-care deep learning framework for covid-19 diagnosis, *ACM Transactions on Multimedia Computing Communications and Applications* 17 (2021) 1–24.
- [47] M. H. Nadimi-Shahraki, H. Zamani, S. Mirjalili, Enhanced whale optimization algorithm for medical feature selection: A covid-19 case study, *Computers in Biology and Medicine* 148 (2022) 105858.
- [48] C. K. Leung, D. L. Fung, D. Mai, Q. Wen, J. Tran, J. Souza, Explainable data analytics for disease and healthcare informatics, in: *25th International Database Engineering & Applications Symposium*, 2021, pp. 65–74.
- [49] D. Q. Nguyen, N. Q. Vo, T. T. Nguyen, K. Nguyen-An, Q. H. Nguyen, D. N. Tran, T. T. Quan, BeCaked: An explainable artificial intelligence model for COVID-19 forecasting, *Scientific Reports* 12 (2022) 1–26.
- [50] M. Smith, F. Alvarez, Identifying mortality factors from machine learning using shapley values—a case of covid19, *Expert Systems with Applications* 176 (2021) 114832.
- [51] L. E. Tideman, L. G. Migas, K. V. Djambazova, N. H. Patterson, R. M. Caprioli, J. M. Spraggins, R. Van de Plas, Automated biomarker candidate discovery in imaging mass spectrometry data through spatially localized shapley additive explanations, *Analytica Chimica Acta* 1177 (2021) 338522.
- [52] Y. R. Xie, D. C. Castro, S. E. Bell, S. S. Rubakhin, J. V. Sweedler, Single-cell classification using mass spectrometry through interpretable machine learning, *Analytical chemistry* 92 (2020) 9338–9347.
- [53] A. Liangou, A. Tasoglou, H. J. Huber, C. Wistrom, K. Brody, P. G. Menon, T. Bebekoski, K. Menschel, M. Davidson-Fiedler, K. DeMarco, et al., A method for the identification of covid-19 biomarkers in human breath using proton transfer reaction time-of-flight mass spectrometry, *EClinicalMedicine* 42 (2021) 101207.
- [54] S. M. Lundberg, B. Nair, M. S. Vavilala, M. Horibe, M. J. Eisses, T. Adams, D. E. Liston, D. K.-W. Low, S.-F. Newman, J. Kim, et al., Explainable machine-learning predictions for the prevention of hypoxaemia during surgery, *Nature Biomedical Engineering* 2 (2018) 749–760.
- [55] S. M. Lundberg, G. Erion, H. Chen, A. DeGrave, J. M. Prutkin, B. Nair, R. Katz, J. Himmelfarb, N. Bansal, S.-I. Lee, From local explanations to global understanding with explainable AI for trees, *Nature Machine Intelligence* 2 (2020) 56–67.
- [56] S. R. Safavian, D. Landgrebe, A survey of decision tree classifier methodology, *IEEE Transactions on Systems, Man, and Cybernetics* 21 (1991) 660–674.
- [57] R. R. Selvaraju, M. Cogswell, A. Das, R. Vedantam, D. Parikh, D. Batra, Grad-cam: Visual explanations from deep networks via gradient-based localization, in: *Proceedings of the IEEE international conference on computer vision*, 2017, pp. 618–626.

- [58] H. Wang, Z. Wang, M. Du, F. Yang, Z. Zhang, S. Ding, P. Mardziel, X. Hu, Score-cam: Score-weighted visual explanations for convolutional neural networks, in: Proceedings of the IEEE/CVF conference on computer vision and pattern recognition workshops, 2020, pp. 24–25.
- [59] L. Breiman, Random forests, *Machine Learning* 45 (2001) 5–32.
- [60] Shimadzu, Axima performance - a highly flexible research-grade mass spectrometer, <https://www.shimadzu.com/an/products/maldi/ms/axima-performance/index.html>, 2022.
- [61] G. J. McLachlan, Discriminant analysis and statistical pattern recognition, volume 544, John Wiley and Sons, 2004.
- [62] C. R. Harris, K. J. Millman, S. J. Van Der Walt, R. Gommers, P. Virtanen, D. Cournapeau, E. Wieser, J. Taylor, S. Berg, N. J. Smith, et al., Array programming with numpy, *Nature* 585 (2020) 357–362.
- [63] W. McKinney, et al., pandas: a foundational python library for data analysis and statistics, *Python for high performance and scientific computing* 14 (2011) 1–9.
- [64] P. Virtanen, R. Gommers, T. E. Oliphant, M. Haberland, T. Reddy, D. Cournapeau, E. Burovski, P. Peterson, W. Weckesser, J. Bright, et al., Scipy 1.0: fundamental algorithms for scientific computing in python, *Nature methods* 17 (2020) 261–272.
- [65] R. J. Tallarida, R. B. Murray, Area under a curve: trapezoidal and simpson’s rules, *Manual of Pharmacologic Calculations* (1987) 77–81.
- [66] I. Shiri, M. Amini, M. Nazari, G. Hajianfar, A. H. Avval, H. Abdollahi, M. Oveisi, H. Arabi, A. Rahmim, H. Zaidi, Impact of feature harmonization on radiogenomics analysis: Prediction of egfr and kras mutations from non-small cell lung cancer pet/ct images, *Computers in biology and medicine* 142 (2022) 105230.
- [67] F. Pedregosa, G. Varoquaux, A. Gramfort, V. Michel, B. Thirion, O. Grisel, M. Blondel, P. Prettenhofer, R. Weiss, V. Dubourg, et al., Scikit-learn: Machine learning in python, *The Journal of Machine Learning Research* 12 (2011) 2825–2830.
- [68] M. Abadi, P. Barham, J. Chen, Z. Chen, A. Davis, J. Dean, M. Devin, S. Ghemawat, G. Irving, M. Isard, et al., {TensorFlow}: a system for {Large-Scale} machine learning, in: 12th USENIX symposium on operating systems design and implementation (OSDI 16), 2016, pp. 265–283.
- [69] S. M. Lundberg, S.-I. Lee, A unified approach to interpreting model predictions, *Proceedings of the 31st International Conference on Neural Information Processing Systems* (2017) 4768–4777.
- [70] A. K. Menon, X. J. Jiang, S. Vembu, C. Elkan, L. Ohno-Machado, Predicting accurate probabilities with a ranking loss, *Proceedings of the International Conference on Machine Learning 2012* (2012) 703.
- [71] J. C. Platt, Probabilistic outputs for support vector machines and comparisons to regularized likelihood methods, *Advances in Large Margin Classifiers* 10 (1999) 61–74.
- [72] L. Ceriani, P. Verme, The origins of the gini index: extracts from variabilità e mutabilità (1912) by corrado gini, *The Journal of Economic Inequality* 10 (2012) 421–443.
- [73] M. T. Ribeiro, S. Singh, C. Guestrin, "why should i trust you?": Explaining the predictions of any classifier, *Proceedings of the 22nd ACM SIGKDD International Conference on Knowledge Discovery and Data Mining* (2016) 1135–1144.
- [74] L. S. Shapley, A value for n-person games, *Contributions to the Theory of Games* 2.28 (1953) 307–317.